Discovery of chalcogenides structures and compositions using mixed fluxes

https://doi.org/10.1038/s41586-022-05307-7

Received: 3 January 2022

Accepted: 1 September 2022

Xiuquan Zhou[1], Venkata Surya Chaitanya Kolluru[2], Wenqian Xu[3], Luqing Wang[2,4], Tieyan Chang[5], Yu-Sheng Chen[5], Lei Yu[2], Jianguo Wen[2], Maria K. Y. Chan[2], Duck Young Chung[1] & Mercouri G. Kanatzidis[1,6]✉

Advancements in many modern technologies rely on the continuous need for materials discovery. However, the design of synthesis routes leading to new and targeted solid-state materials requires understanding of reactivity patterns[1–3]. Advances in synthesis science are necessary to increase efficiency and accelerate materials discovery[4–10]. We present a highly effective methodology for the rational discovery of materials using high-temperature solutions or fluxes having tunable solubility. This methodology facilitates product selection by projecting the free-energy landscape into real synthetic variables: temperature and flux ratio. We demonstrate the effectiveness of this technique by synthesizing compounds in the chalcogenide system of A(Ba)-Cu-Q(O) (Q = S or Se; A = Na, K or Rb) using mixed AOH/AX (A = Li, Na, K or Rb; X = Cl or I) fluxes. We present 30 unreported compounds or compositions, including more than ten unique structural types, by systematically varying the temperature and flux ratios without requiring changing the proportions of starting materials. Also, we found that the structural dimensionality of the compounds decreases with increasing reactant solubility and temperature. This methodology serves as an effective general strategy for the rational discovery of inorganic solids.

The extent of control and predictability of synthetic outcomes for extended solids composed of more than three elements compared with that for many molecular compounds is low. Consequently, exploratory synthesis is an invaluable tool for materials discovery—as the pioneer in this field, John Corbett, described, "It is always difficult to predict the unimaginable"[11]. Owing to the knowledge accumulating from exploratory synthesis and the progress made during the past decades[1,12], predictive synthesis[13], including identifying composition and structure that confer the desired properties and synthesizing the desired targets, may soon be within reach. However, this requires the ability to understand and predict viable reaction pathways. Therefore, new synthetic strategies to show effective reaction pathways that can add a more 'rational' component to exploratory synthesis are required to accelerate materials discovery and achieve the ultimate goal—synthesizable materials by design.

We present a more generalized synthesis methodology that can be adapted to control the reaction paths and phase selection to achieve the synthesis of a diverse set of compounds while simultaneously extracting generalized rules and trends in stoichiometry, as well as structure assembly and dimensionality. We demonstrate the effectiveness of this approach in the A(Ba)-Cu-Q(O) system using hydroxide/halide mixtures by synthesizing 30 unreported compounds, including more than ten unique structure types. Furthermore, we describe a strategy to control the structural dimensionality of the products and preserve the building blocks to synthesize compounds with unique structure types. We also demonstrate how this knowledge can be used to select reaction paths to obtain targeted solid-state compounds with challenging structural characteristics, such as mixed anions, by tuning the solubility of a mixed flux.

Reactivity trends with tunable flux

The solubility can be methodically controlled by using a mixed flux comprising an effective solvent to ensure high solubility and an anti-solvent to modulate the solubility. To synthesize chalcogenide systems in particular, we selected AOH and AX as the tunable flux components because the solubility of alkali chalcogenides can be two to three orders of magnitude larger in AOH than in AX[14,15]. Therefore, the AX component fine-tunes the solubility, whereas the identity of A serves to fine-tune the basicity of the flux, which independently influences the solubility and reactivity of chalcogenides. The solubility of the reactants can be further controlled by using mixed alkali ions in the hydroxide. Therefore, for a ternary $A_xM_yQ_z$ (M = transition metals) system using mixed AOH/AX fluxes, we expect the stoichiometric ratio of x/y in the crystallizing solids to be controllable using the solubility. This would have a profound effect on the structure because the incorporation of a large number of Q^{2-} atoms (which would increase the number of counter cations) will probably reduce the dimensionality from 3D to

---

[1]Materials Science Division, Argonne National Laboratory, Lemont, IL, USA. [2]Center for Nanoscale Materials, Argonne National Laboratory, Lemont, IL, USA. [3]X-ray Science Division, Advanced Photon Source, Argonne National Laboratory, Lemont, IL, USA. [4]The Materials Research Center, Northwestern University, Evanston, IL, USA. [5]NSF's ChemMatCARS, The University of Chicago, Lemont, IL, USA. [6]Department of Chemistry, Northwestern University, Evanston, IL, USA. ✉e-mail: m-kanatzidis@northwestern.edu

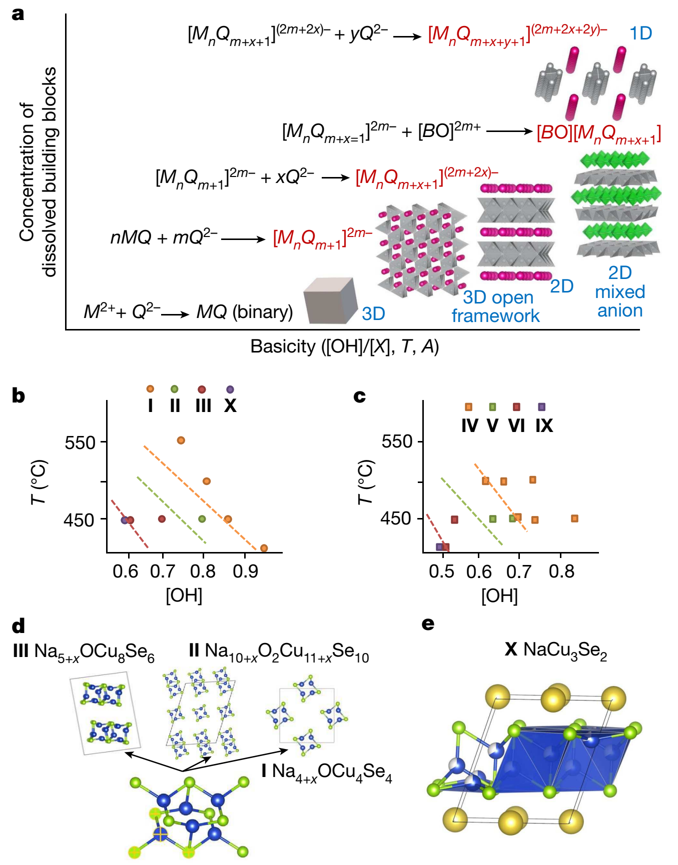

Fig. 1 | Compositional and dimensionality control with basicity. **a**, Organizational reaction-trend diagram showing the effect of increasing basicity (which is a function of flux ratio, temperature and alkali ion type) on the successive formation of soluble species (in red font) resulting from the attack of Q^{2-} ions on low-dimensional species. These fragments provide the building blocks for crystalline compounds. The higher the basicity (further right along the *x*-axis), the higher the solubility and the concentration of low-dimensional fragments (further up the *y*-axis). The structures show the products crystallized under those conditions of basicity. The diagram also shows the perturbation of the reaction path in the presence of further metal ions (such as *B*) and the formation of mixed-anion structures (provided that *B* is an oxophilic element). **b**,**c**, Syntheses in the mixed flux of NaOH/NaI with *T*/[OH] phase diagram for *Q* = Se (**b**) and phase diagram for *Q* = S (**c**). The dotted lines in **b** and **c** are estimated phase boundaries. **d**, Crystal structures of **I** ($Na_{4+x}OCu_4Se_4$), **II** ($Na_{10+x}O_2Cu_{11+x}Se_{10}$) and **III** ($Na_{5+x}OCu_8Se_6$). **e**, Compound **X** ($NaCu_3Se_2$). Compounds **IV** ($Na_{4+x}OCu_4S_4$), **V** ($Na_{10+x}O_2Cu_{11+x}S_{10}$) and **VI** ($Na_{5+x}OCu_8S_6$) are isostructural with **I**, **II** and **III**, respectively. Yellow, light green and blue spheres represent Na, Se and Cu atoms, respectively.

0D, as illustrated in Fig. 1a (refs. [1,16]). The strategy proved to be effective, considering that 30 unreported compounds were synthesized, as listed in Table 1. We detail the reaction trend with the results obtained using the NaOH/NaI flux below. A similar trend was observed for reactions in (Na, Li)OH/NaI, (K, Li)OH/NaI (Extended Data Fig. 1) and (Rb, Li)OH/NaI (Extended Data Fig. 1), which are detailed in Methods.

From reactions in NaOH/NaI at 400–550 °C with [OH] = 0.5–1, for *Q* = Se and S, we obtained eight unreported phases (**I**–**VI**, **IX** and **X**) by adjusting the temperature (*T*) and [OH]. The phase diagrams showing the *T*/[OH] regions of each phase are illustrated in Fig. 1b,c. For *Q* = Se at 450 °C, we observed the formation of **I** ($Na_{4+x}OCu_4Se_4$), **II** ($Na_{10+x}O_2Cu_{11+x}Se_{10}$) and **III** ($Na_{5+x}OCu_8Se_6$) at [OH] = 0.85, 0.80 and 0.70, respectively (Fig. 1d and Fig. S1). The structure of **I** ($Na_{4+x}OCu_4Se_4$) (Fig. 1d, right) consists of chains of Cu_4Se_4 formed by corner-sharing triangular CuS_3 and $Na_{4+x}O$ ($x \approx 0.4$), a 1D fragment from a NaCl-type structure with infinite corner-sharing ONa_6 octahedra. This structure type is similar to the $Nb_5Cu_4Si_4$ type, except that the octahedral centre of Nb is empty[17]. The structures of **II** (Fig. 1d, middle) and **III** (Fig. 1d, left) correspond to *n* = 2 and 3, respectively, in the homologous series of **I** (*n* = 1) with chains of $Cu_{2+2n}Se_{3+n}$.

When [OH] was decreased to 0.6, the products obtained were a mixture of **III** ($Na_{5+x}OCu_8Se_6$) and **X** ($NaCu_3Se_2$, Fig. 1e). The structure of **X** ($NaCu_3Se_2$) consists of two types of Cu–Se coordination: triangular and tetrahedral. In **X**, Na and Se form a CdI_2-type 2D honeycomb lattice and Cu can occupy the tetrahedral sites between the two adjacent Se sheets or the triangular sites within each Se honeycomb plane. All Cu sites are disordered, with partial occupancies summing to three Cu atoms to charge balance with one Na and two Se atoms. These results clearly show a similar trend of phase evolution as a function of the flux ratio as for K/Ni/S in mixed LiOH/KOH (ref. [18]). Notably, when the solubility was increased by using a lower NaOH/NaI ratio, the dimensionality of the products decreased in the order **X**, **III**, **II** and **I** as the Cu/Na ratio decreased. This entirely agrees with our hypothesis that increasing the solubility and A_2Q concentration can lead to a larger ratio of *x*/*y* in $A_xM_yQ_z$ and reduce the dimensionality. For reactions occurring at temperatures exceeding 450 °C, only **I** ($Na_{4+x}OCu_4Se_4$) was observed for [OH] as low as 0.75. Considering that the solubility increases with *T*, it is probable that the overall solubility is higher, despite the reduction in [OH].

For *Q* = S at 450 °C, when [OH] was 0.68, the reaction produced a mixture of **IV** ($Na_{4+x}OCu_4S_4$) and **V** ($Na_{10+x}O_2Cu_{11+x}S_{10}$), although only **IV** was observed for [OH] > 0.7 (Fig. S2a,b). Only **V** was obtained when [OH] was further reduced to 0.62 (Fig. 1c and Fig. S2c). The structure of **IV** is identical to its Se analogue **I** (Fig. 1d, right), whereas the structure of **V** is a slightly disordered version of **II** (Fig. 1d, middle), reducing its symmetry from *C*2/*m* to *P*2/*c*. To obtain the sulfide analogues of **III** or **X**, the solubility or temperature required further reduction. When [OH] was reduced to 0.55 at 450 °C, the double-chained sulfide **VI** ($Na_{5+x}OCu_8S_6$) was obtained (Fig. S2d). However, pure 2D $NaCu_3S_2$ (**IX**) was not obtained for [OH] as low as 0.5 at 400 °C, at which a mixture of **IX** ($NaCu_3S_2$) and **VI** ($Na_{5+x}OCu_8S_6$) was produced. This is probably owing to the higher solubility of sulfides than that of selenides in NaOH/NaI.

Perturbation of reaction path

When further elements such as Ba were introduced during the reaction, we observed different outcomes involving both ternary Ba/Cu/*Q* and quaternary Ba/*A*/Cu/*Q* compounds. On the basis of our hypothesis, the formation of Ba/*A*/Cu/*Q* is preferred at high reactant solubility and temperature, because the solubility of quaternary products is generally lower than that of ternary products. Through the reactions performed using the LiOH/LiCl flux, we only obtained α-$BaCu_2Se_2$ (Fig. 2a) at *T* = 450 and 500 °C, [OH] = 0.6–0.9. However, for *Q* = S at 450 °C, the product was α-$BaCu_2S_2$ (Fig. 2a) at [OH] = 0.6, whereas at [OH] = 0.75, $ThCr_2Si_2$-type β-$BaCu_{1.4}Li_{0.6}S_2$ (**XIV**, Fig. 2b) was obtained. Li substitution was probably caused by the more favourable entropy of mixing in the product, similar to that in $Na(Cu_{0.6}Li_{0.4})S$ (**XII**). However, unlike the 40% substitution in **XII**, the lower substitution (30%) in $BaCu_{1.4}Li_{0.6}S_2$ (**XIV**) is attributed to the lower synthesis temperature of 450 °C (instead of 500 °C).

We also controlled the reaction outcome by tuning the Na/Li ratio in (Na, Li)OH/NaI. For *Q* = S with Na/Li = 1, [OH] = 0.85 and *T* = 500 °C, instead of β-$BaCu_{2-x}Li_xS_2$, the product was an unreported mixed-anion compound, **XIX** ($Ba_{4.5}Cu_{6.7}Na_{1.7}O_4S_6$, Fig. 2c). Its structure type is unique, featuring an immense 1D infinite channel having a diameter of about 12 Å enclosed by four slabs of 7 × ∞ edge-sharing CuS_4 tetrahedra. The large cavity is filled with an exotic structure of $Ba_{4.5}Na_{1.7}O_4$ consisting of a face-sharing CsCl-type BaO_8 1D chain in the centre. The following shell surrounding the chain consists of four edge-sharing fluorite-type NaO_4 connecting the third shell of distorted face-sharing CsCl-type

Table 1 | New phases synthesized by controlling the reaction paths using mixed *A*OH/*AX* fluxes under selected synthetic conditions

Code	Formula	Space group	Structure type	Coordination	Dimension	Flux	[OH]	*T* (°C)
I	$Na_{4+x}OCu_4Se_4$	*I*4/*m*	$Nb_5Cu_4Si_4$	Tr	1D	NaOH/NaI	0.85	500
II	$Na_{10+x}O_2Cu_{11+x}Se_{10}$	*C*2/*m*	Unique	Tr, Tet	1D	NaOH/NaI	0.80	450
III	$Na_{5+x}OCu_8Se_6$	*C*2/*m*	Unique	Tr, Tet	1D	NaOH/NaI	0.70	450
IV	$Na_{4+x}OCu_4S_4$	*I*4/*m*	$Nb_5Cu_4Si_4$	Tr	1D	NaOH/NaI	0.80	450
V	$Na_{10+x}O_2Cu_{11+x}S_{10}$	*P*2/*c*	Unique	L, Tr, Tet	1D	(Na, Li)OH/NaI	0.68	450
VI	$Na_{5+x}OCu_8S_6$	*C*2/*m*	Unique	Tr, Tet	1D	NaOH/NaI	0.50	400
VII	$K_{4+x}OCu_4S_4$	*I*4/*m*	$Nb_5Cu_4Si_4$	Tr	1D	(K, Li)OH/KI	0.75	450
VIII	$K_{4+x}OCu_4Se_4$	*I*4/*m*	$Nb_5Cu_4Si_4$	Tr	1D	(K, Li)OH/KI	0.80	500
IX	$NaCu_3S_2$	*R*-3*m*	Unique	Tr, Tet	2D	(Na, Li)OH/NaI	0.68	500
X	$NaCu_3Se_2$	*C*2/*m*	Unique	Tr, Tet	2D	(Na, Li)OH/NaI	0.85	450
XI	KCu_3S_2	*R*-3*m*	Unique	Tr, Tet	2D	(K, Li)OH/KI	0.80	600
XII	$Na(Cu_{0.6}Li_{0.4})S$	*P*4/*nmm*	PbClF	Tet	2D	(Na, Li)OH/NaI	0.90	500
XIII	$Na(Cu_{0.6}Li_{0.4})Se$	*P*4/*nmm*	PbClF	Tet	2D	(Na, Li)OH/NaI	0.85	600
XIV	$BaCu_{1.4}Li_{0.6}S_2$	*I*4/*mmm*	$ThCr_2Si_2$	Tet	2D	LiOH/LiCl	0.75	450
XV	$(Ba_{0.44}Rb_{0.56})Cu_2Se_2$	*I*4/*mmm*	$ThCr_2Si_2$	Tet	2D	(Rb, Li)OH/RbI	0.60	450
XVI	$Na_3BaCu_7S_6$	*C*2/*m*	Unique	L, Tr	2D	(Na, Li)OH/NaI	0.75	500
XVII	$K_3BaCu_7S_6$	*C*2/*m*	Unique	L, Tr	2D	LiOH/KOH	1.00	450
XVIII	$Ba_2Cu_2Na_{1.3}O_{1.1}S_3$	*C*2/*m*	Unique	Tr, Tet	2D	(Na, Li)OH/NaI	0.85	420
XIX	$Ba_{4.5}Cu_{6.7}Na_{1.7}O_4S_6$	*I*4/*m*	Unique	Tet	ps-1D	(Na, Li)OH/NaI	0.68	500
XX	$Ba_{2-x}Cu_{5.5}OSe_4$	*Pnma*	Unique	Tr, Tet	ps-1D	(Na, Li)OH/NaI	0.85	450
XXI	$Ba_2Cu_{0.8}O_2Cu_2Se_2$	*I*4/*mmm*	Heterolayer	Tet	2D	(Na, Li)OH/NaI	0.75	450
XXII	$Ba_2Na_{0.55}O_2Cu_2Se_2$	*I*4/*mmm*	Heterolayer	Tet	2D	(Na, Li)OH/NaI	0.80	450
XXIII	$(Ba_{1.63}K_{0.37})O_2Cu_2Se_2$	*I*4/*mmm*	Heterolayer	Tet	2D	(K, Li)OH/KI	0.70	450
XXIV	$Ba_2Cu_{0.8}O_3CuS$	*P*4/*nmm*	Heterolayer	Tet	2D	(K, Li)OH/KI	0.80	600
XXV	KCu_5Se_3	$P4_2/mnm$	$CsAg_5Te_3$	Tr, Tet	ps-1D	(K, Li)OH/KI	0.85	500
XXVI	$RbCu_{7-x}Se_4$	*I*4/*m*	Unique	Tr, Tet	ps-1D	(Rb, Li)OH/RbI	0.75	450
XXVII	$Ba_4Rb_6Cu_{12}Se_{13}$	*Im*-3*m*	Unique	Tet	0D	(Rb, Li)OH/RbI	0.75	450
XXVIII*	$Na_3Cu_4Se_4$	*Pbam*	$K_3Cu_4S_4$	Tr	1D	(Na, Li)OH/NaI	0.60	550
XXIX	$BaK_2Cu_4S_{4-x}Se_x$	*Pbam*	$K_3Cu_4S_4$	Tr	1D	(K, Li)OH/KaI	0.70	600
XXX	$BaK_2Cu_8S_6$	*C*2/*m*	$Rb_3Cu_8Se_6$	Tr, Tet	2D	LiOH/KOH	1.00	450

The reactant to flux ratios were not varied, and the temperature and hydroxide concentrations are the only determining factors for the selection of products. L, Tr and Tet represent linear, triangular and tetrahedral coordination for Cu bonding, respectively, and ps-1D denotes the pseudo-1-dimensional structure type. Compound **XXVIII** marked with * was recovered from panoramic synthesis, which was carried out in a carbon-coated silica tube instead of a glassy carbon boat. Crystal structures are provided in the Supplementary Data in the form of crystallographic information files (CIFs) except for **VII** and **XI** and available at the Cambridge Crystallographic Data Centre (CCDC) database with deposition numbers CSD 2184424–2184451.

BaO_4S_4 (edge centre of the cavity) and BaO_2S_6 (corner of the cavity). This unique structure type consists of large fragments of anti-PbO layers from β-$BaCu_2S_2$.

For Q = Se with Na/Li = 0.15 and [OH] = 0.85 at 450 °C, the product was an unreported mixed-anion compound, **XX** ($Ba_{2-x}Cu_{5.5}OSe_4$ Fig. 2d); it has a tunnel-type structure similar to that of **XIX** ($Ba_{4.5}Cu_{6.7}Na_{1.7}O_4S_6$, Fig. 2c) although with smaller cavities and no Na incorporation. The channel is filled with edge-sharing 7-coordinated BaO_3Se_4, which resembles the Ba-O coordination in $Ba(OH)_2$ (ref. [19]). Fragments of anti-PbO-type $CuSe_4$ edge-sharing tetrahedra are preserved in this mixed-anion open-channel structure of **XX** ($Ba_{2-x}Cu_{5.5}OSe_4$) because they enclose these channels. The more basic flux, composed of RbOH at Rb/Li = 1 and [OH] = 0.6 at 450 °C, produced **XV** $(Ba_{0.44}Rb_{0.56})Cu_2Se_2$ (Fig. 2e), which is isostructural with β-$BaCu_2Se_2$ except for a noticeable substitution of Rb to the Ba site. Such large alkali substitution has never been reported, and the highest value reported so far was 36% for $(Ba_{0.64}K_{0.36})Cu_2S_2$ (ref. [20]). It seems that pseudo-1-dimensional (ps-1D) structures such as **XIX** ($Ba_{4.5}Cu_{6.7}Na_{1.7}O_4S_6$) and **XX** ($Ba_{2-x}Cu_{5.5}OSe_4$) are intermediates to 2D structures exhibiting fragments from anti-PbO-type layers. Compared with the condition (Na/Li = 0.15 and [OH] = 0.85 at 450 °C) that formed **XX** ($Ba_{2-x}Cu_{5.5}OSe_4$) using (Na, Li)OH/NaI, when the solubility was increased by increasing Na/Li to 2, ps-1D **XX** was bypassed and **XXII** ($Ba_2Na_{0.55}O_2Cu_2Se_2$) was obtained. For a similar reaction in (K, Li)OH/KI with K/Li = 2 and [OH] = 0.7, **XXIII** $(Ba_{1.63}K_{0.37})O_2Cu_2Se_2$ was formed (Fig. 2f).

When the solubility is sufficiently high to favour mixed-anion structures such as **XXII** and **XXIII**, further perturbations with other transition metals (M) will produce $Ba_2MO_2Cu_2Q_2$. For example, when a Cu(II) source, such as CuO, was introduced to the reaction that resulted in **XXII** ($Ba_2Na_{0.55}O_2Cu_2Se_2$), the product obtained was **XXI** ($Ba_2Cu_{0.8}O_2Cu_2Se_2$, Fig. 2j). When Se was replaced with S under identical conditions, the product was $Ba_2Cu_{0.8}O_2Cu_2S_2$ (isostructural to **XXI**). The preparation of these compounds may be difficult, considering that $Ba_2CuO_2Cu_2Se_2$ was only prepared under high pressure (5.5 GPa) at 1,000 °C (ref. [21]), whereas the sulfide analogue $Ba_2CuO_2Cu_2S_2$ has not been reported. Furthermore, when the reaction temperature was increased to 500–550 °C, we observed alkali substitution at the Ba site, resulting in products such as $[(Ba_{1.8}K_{0.2})Cu_{0.8}O_2][Cu_2Se_2]$, which shows promise for tuning

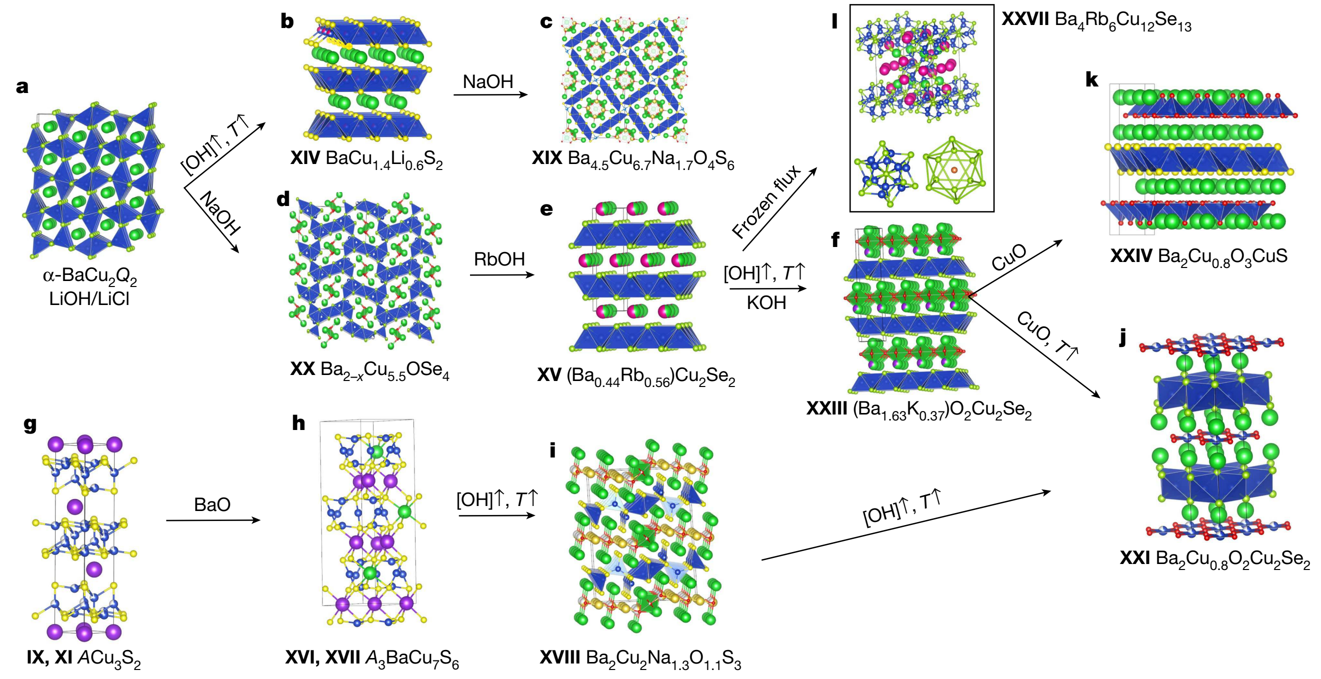

Fig. 2 | Perturbation of reaction pathways when BaO is present. **a**, α-$BaCu_2Q_2$. **b**, **XIV** β-$BaCu_{1.4}Li_{0.6}S_2$. **c**, **XIX** $Ba_{4.5}Cu_{6.7}Na_{1.7}O_4S_6$. **d**, **XX** $Ba_{2-x}Cu_{5.5}OSe_4$. **e**, **XV** $(Ba_{0.44}Rb_{0.56})Cu_2Se_2$. **f**, **XXIII** $(Ba_{1.63}K_{0.37})O_2Cu_2Se_2$. **g**, **IX**, **XI** ACu_3S_2. **h**, **XVI**, **XVII** $A_3BaCu_7S_6$. **i**, **XVIII** $Ba_2Cu_2Na_{1.3}O_{1.1}S_3$. **j**, **XXI** $Ba_2Cu_{0.8}O_2Cu_2Se_2$. **k**, **XXIV** $Ba_2Cu_{0.8}O_3CuS$. **l**, The 0D cluster compound **XXVII** $Ba_4Rb_6Cu_{12}Se_{13}$. Yellow, purple, pink, blue, green, red, light yellow and light green spheres represent Na, K, Rb, Cu, Ba, O, S and Se atoms, respectively. The bottom-left and bottom-right insets in **l** illustrate the $[Cu_{12}Se_{13}]^{14-}$ cluster and the icosahedron enclosing Se_{13}, respectively, in which the Se atoms at the vortices and centre of the icosahedron are shown in light green and orange, respectively.

the oxidation state of Cu in the oxide layer, because the oxidation state of high-critical-temperature cuprate exceeds +2. Furthermore, when the reaction temperature increased to 700 °C, an unknown compound formed where the oxide layer is the '$Ba_2Cu_{0.8}O_3$' (**XXIV**, $Ba_2Cu_{0.8}O_3CuS$), as shown in Fig. 2k. This suggests a trend wherein the solubilities of M_nQ_m chalcogenide building blocks and M_qQ_p oxide blocks increase with p/q, as illustrated in Fig. 1a. Therefore, the method using tunable solubility to control the stoichiometry and dimensionality of $A_xM_yQ_z$ is probably a general approach that functions for non-chalcogenides.

Furthermore, we tested the effect of Ba^{2+} perturbation on the synthetic pathways that form **IX** ($NaCu_3S_2$) and **XI** (KCu_3S_2), as shown in Fig. 2g. When BaO was introduced, the reaction path changed, producing **XVI** ($Na_3BaCu_7S_6$) and **XVII** ($K_3BaCu_7S_6$, Fig. 2h). They exhibit a unique type of structure featuring corner-sharing triangular CuS_3 and linearly coordinated CuS_2 units. Notably, these linearly coordinated Cu atoms form a kagome (k) layer, whereas the two adjacent triangularly coordinated Cu atoms form two honeycomb (h) layers, thereby resulting in a hkh-type hybrid honeycomb and kagome lattice. When the solubility was further increased using (Na, Li)OH/NaI, the product was an unreported type of mixed-anion compound, **XVIII** ($Ba_2Cu_2Na_{1.3}O_{1.1}S_3$, Fig. 2i), consisting of alternating Cu_2S_3 chalcogenide layers and $Ba_2Na_{1.3}O_{1.1}$ oxide layers. Each Cu_2S_3 layer comprises chains of edge-sharing CuS_4 tetrahedra connected by parallel triangular CuS_3 units.

Linking flux conditions to stability

To apply this mixed-flux method for materials design, we need a deeper understanding of the correlation between the stability of the products and synthetic conditions. Hence, we carried out panoramic syntheses using in situ powder X-ray diffraction (PXRD). The results (detailed in Methods) are shown in Extended Data Fig. 3 and Fig. S4. The corresponding temperature profiles are shown in Fig. S3. Overall, the panoramic syntheses results were consistent with our ex situ reactions for the phase evolution over basicity. Furthermore, it showed several unknown intermediates and unreported phases (at least eight, marked with A–H in Extended Data Fig. 3). With its help, we could identify an unreported composition, $Na_3Cu_4Se_4$ (**XXVIII**). We observed that, once the flux is molten, the binary precursors dissolve in the flux immediately and start to precipitate. The products formed at lower temperatures will re-dissolve and re-precipitate. The addition of an oxide base can affect the solubility as well, which is explained by the Lux[22] and Flood[23] basicity theory of molten hydroxide. For example, the dissolving ability of the flux increases with the addition of BaO, as we see complete dissolution. This is why when a perturbation with a strong base such as BaO was introduced, it allowed a diverse range of structures to be made.

With the addition of BaO, we also observed a highly unusual phenomenon: the precipitate (**IV**, $Na_{4+x}OCu_4S_4$) dissolved completely when the temperature increased from 400 °C to 450 °C and then recrystallized to **XVI** ($Na_3BaCu_7S_6$) when holding at 450 °C over time (diffraction data in Fig. 3a and Extended Data Fig. 3d). We try to analyse this process with free energy (ΔG) using thermodynamic concepts, as shown in the bottom half of Fig. 3a. At equilibrium with $T = 400$ °C, the stable phase is α (**IV**), whereas phase β (**XVI**) is metastable. Furthermore, complete dissolution of α at this temperature is clearly unfavourable in free energy compared with solution (sol.) + α. Their relative positions in the energy landscape are reflected in Fig. 3a, left. Because α was dissolved completely when the temperature increased to 450 °C, the dissolution of α was spontaneous at 450 °C. Therefore, at 450 °C, the change in ΔG from sol. + α to sol. (complete dissolution) is negative. Thus, we adjust the new-free energy landscape in Fig. 3a, middle accordingly to show sol. at lower energy compared with (sol.) + α. However, because β was able to crystallize by holding at 450 °C, it suggests that (sol). is probably a metastable condition and the free energy of (sol.) + β should be lower than the complete solution (sol.). Therefore, we observed the crystallization of β in Fig. 3a, right.

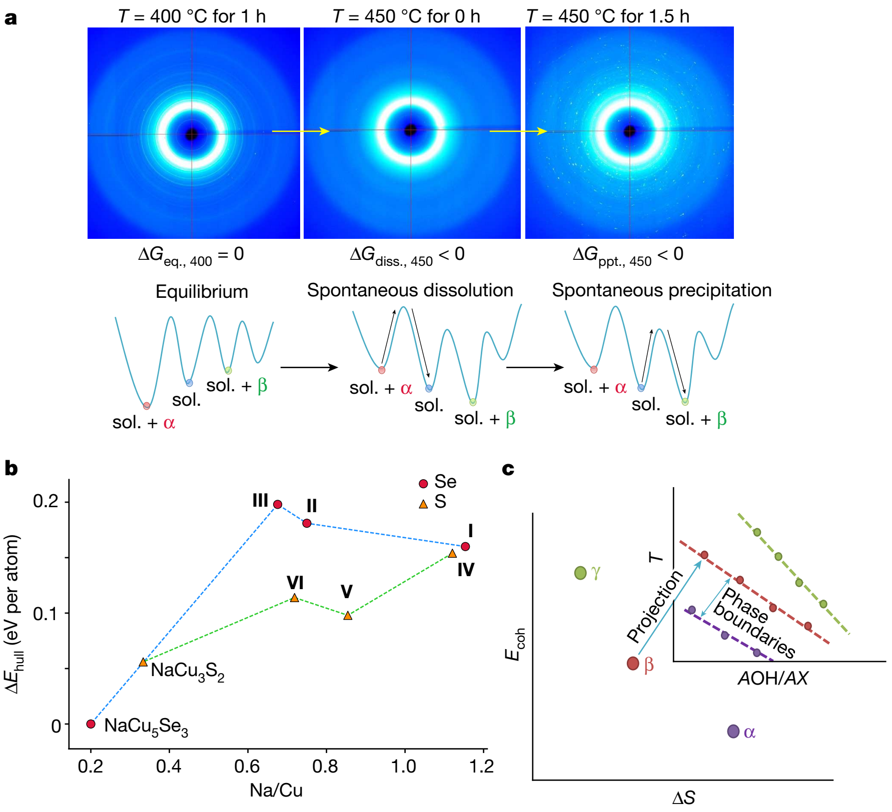

Fig. 3 | Projecting the energy landscape onto synthetic parameters. a, X-ray scattering patterns at three temperatures showing conversion from α (**IV**) to β (**XVI**) and corresponding changes of the free-energy landscape during the dissolution of **IV** and recrystallization of **XVI**, shown below. **b**, DFT calculations of the formation energies of the heterochains **I**–**VI**, **IX** ($NaCu_3S_2$) and $NaCu_5S_3$. ΔE_{hull} denotes the energy above the convex hull and a value of 0 indicates stability against decomposition into other known phases. **c**, Diagrams showing how the free-energy landscape can be projected onto synthetic variables (inset). Cohesive energy (E_{coh}) is the absolute value of enthalpy ($-H$), and the larger the value, the stronger the bonding energy of a compound. The cohesive energy and entropy of the products α, β and γ with decreasing dimensionality and increasing Na/Cu ratio tend to decrease with increasing entropy, which is favoured at higher temperatures or *A*OH/*AX* ratios. This is projected synthetically by increasing the temperature or basicity (*A*OH/*AX* ratio), as illustrated in the inset.

To gain further insights into the thermodynamics, we correlate the phase stability of the products (ΔE_{hull}) with Na/Cu ratio (or dimensionality) using density functional theory (DFT) calculations on the heterochains **I**–**VI**, **IX** ($NaCu_3S_2$) and $NaCu_5S_3$. The calculations showed a trend that product stability (ΔE_{hull}) decreased with decreasing dimensionality and increasing Na/Cu ratio in our synthesis (Fig. 3b). Moreover, many of the heterochains, such as **I**–**V**, exhibit an energy above the convex hull (ΔE_{hull}) between 100 and 200 meV per atom. A recent summary of 24,526 compounds[24] showed an average ΔE_{hull} of 32–40 meV per atom, with 90% of them below 100 meV per atom. The large values of ΔE_{hull} for the heterochains suggest high probability of metastability. One possibility is that the stabilization of these heterochains is driven by entropy, considering that higher temperature or solubility (from higher [OH]) favoured their formation. Therefore, increasing temperature or solubility in these tunable mixed fluxes favours products with lower cohesive or lattice energy ($E_{coh} = -H$) and higher entropy. However, we want to emphasize that this is a general trend instead of a precise rule because this trend is a reflection of the free-energy change of the system as a whole (precipitate + solution) not just the precipitate, as demonstrated by the dissolution and reprecipitation process (Fig. 3a). When the dissolving power of the flux is low, the outcome is very similar to conventional solid state. This is because with low solubility, the contribution to the free-energy landscape of the solution from the products is negligible. Thus, we can rationalize product selection and structure dimensionality control in the tunable mixed flux, in which the free-energy landscape using cohesive energy E_{coh} and entropy change ΔS of the products (Fig. 3c) can be projected onto synthetic variables such as temperature and *A*OH/*AX* ratio (Fig. 3c, inset). It is expected that products with lower cohesive energy and higher entropy are selected with increasing temperature or higher solubility, as depicted in Fig. 3c, inset, and their free-energy profile as a function of increasing temperature or *A*OH/*AX* ratio becomes closer and closer to a complete solution (sol.).

The science of synthesis that shows the productive reaction pathways to new compounds and its generalization over broad classes of systems is greatly underdeveloped. This work is an effort to advance this science. Our results, with 30 new compounds rationally discovered using mixed *A*OH/*AX* fluxes, demonstrate that product selection becomes possible by projecting the free-energy landscape[25,26] onto synthetic variables. This synthetic strategy can be used to rationally enhance the effectiveness of exploratory syntheses by widening the phase regions and reducing the number of synthetic parameters because temperature and flux ratio are the only determining factors. We also demonstrated that certain building blocks or fragments could be preserved in unique structures by introducing a perturbation to known synthetic conditions. This can be used to target new structures having the desired building blocks. Finally, the proposed method has the potential to yield useful reaction rules and patterns and serve as a rational approach for the guided discovery synthesis of a wide range of materials, although its translational value in other flux systems, such as mixed-metal fluxes, requires further validation.

Online content

Any methods, additional references, Nature Research reporting summaries, source data, extended data, supplementary information, acknowledgements, peer review information; details of author contributions and competing interests; and statements of data and code availability are available at https://doi.org/10.1038/s41586-022-05307-7.

1. Kanatzidis, M. G. Discovery-synthesis, design, and prediction of chalcogenide phases. *Inorg. Chem.* **56**, 3158–3173 (2017).
2. Shoemaker, D. P. et al. Understanding fluxes as media for directed synthesis: in situ local structure of molten potassium polysulfides. *J. Am. Chem. Soc.* **134**, 9456–9463 (2012).
3. Haynes, A. S., Stoumpos, C. C., Chen, H., Chica, D. & Kanatzidis, M. G. Panoramic synthesis as an effective materials discovery tool: the system Cs/Sn/P/Se as a test case. *J. Am. Chem. Soc.* **139**, 10814–10821 (2017).
4. Nunn, W. et al. Novel synthesis approach for "stubborn" metals and metal oxides. *Proc. Natl Acad. Sci. USA* **118**, e2105713118 (2021).
5. Sanchez-Lengeling, B. & Aspuru-Guzik, A. Inverse molecular design using machine learning: generative models for matter engineering. *Science* **361**, 360–365 (2018).
6. Schmidt, J., Marques, M. R. G., Botti, S. & Marques, M. A. L. Recent advances and applications of machine learning in solid-state materials science. *NPJ Comput. Mater.* **5**, 83 (2019).
7. Oganov, A. R., Pickard, C. J., Zhu, Q. & Needs, R. J. Structure prediction drives materials discovery. *Nat. Rev. Mater.* **4**, 331–348 (2019).
8. Alberi, K. et al. The 2019 materials by design roadmap. *J. Phys. D Appl. Phys.* **52**, 013001 (2018).
9. Tang, F., Po, H. C., Vishwanath, A. & Wan, X. Efficient topological materials discovery using symmetry indicators. *Nat. Phys.* **15**, 470–476 (2019).
10. Tabor, D. P. et al. Accelerating the discovery of materials for clean energy in the era of smart automation. *Nat. Rev. Mater.* **3**, 5–20 (2018).
11. Corbett, J. D. Exploratory synthesis in the solid state. Endless wonders. *Inorg. Chem.* **39**, 5178–5191 (2000).
12. Arachchige, I. U. et al. Mercouri G. Kanatzidis: excellence and innovations in inorganic and solid-state chemistry. *Inorg. Chem.* **56**, 7582–7597 (2017).
13. Kovnir, K. Predictive synthesis. *Chem. Mater.* **33**, 4835–4841 (2021).
14. Chiotti, P. & Markuszewski, R. Binary systems sodium sulfide-sodium hydroxide and sodium carbonate-sodium hydroxide. *J. Chem. Eng. Data* **30**, 197–201 (1985).
15. Seefuth, R. N. & Sharma, R. A. Solubility of Li_2 S in LiCl - KCl melts. *J. Electrochem. Soc.* **135**, 796 (1988).
16. Androulakis, J. et al. Dimensional reduction: a design tool for new radiation detection materials. *Adv. Mater.* **23**, 4163–4167 (2011).
17. Ganglberger, E. Die Kristallstruktur von $Nb_5Cu_4Si_4$. *Monatsh. Chem. Chem. Mon.* **99**, 549–556 (1968).
18. Zhou, X. et al. New compounds and phase selection of nickel sulfides via oxidation state control in molten hydroxides. *J. Am. Chem. Soc.* **143**, 13646–13654 (2021).
19. Friedrich, A., Kunz, M., Miletich, R. & Pattison, P. High-pressure behavior of Ba(OH)2 phase transitions and bulk modulus. *Phys. Rev. B* **66**, 214103 (2002).
20. Zhang, X., Hogan, T., Kannewurf, C. R. & Kanatzidis, M. G. Sulfur p-band hole generation in β-$BaCu_2S_2$. Synthesis of metallic $K_xBa_{1-x}Cu_2S_2$ from molten mixed K·Ba polysulfide salts. *J. Alloys Compd.* **236**, 1–5 (1996).
21. Li, W. et al. Synthesis, structure, and properties of the layered oxyselenide $Ba_2CuO_2Cu_2Se_2$. *Inorg. Chem.* **57**, 5108–5113 (2018).
22. Lux, H., Kuhn, R. & Niedermaier, T. Reaktionen und Gleichgewichte in Alkalihydroxydschmelzen. III. Peroxydgleichgewichte. *Z. Anorg. Allg. Chem.* **298**, 285–301 (1959).
23. Flood, H. & Förland, T. The acidic and basic properties of oxides. *Acta Chem. Scand.* **1**, 592–606 (1947).
24. Pöhls, J.-H., Heyberger, M. & Mar, A. Comparison of computational and experimental inorganic crystal structures. *J. Solid State Chem.* **290**, 121557 (2020).
25. Jansen, M. A concept for synthesis planning in solid-state chemistry. *Angew. Chem. Int. Edn* **41**, 3746–3766 (2002).
26. Jansen, M. & Schön, J. C. "Design" in chemical synthesis—an illusion? *Angew. Chem. Int. Edn* **45**, 3406–3412 (2006).

Methods

DFT calculations

DFT calculations were performed using the Vienna Ab initio Simulation Package (VASP)[27–29] with the Perdew–Burke–Ernzerhof[30] generalized gradient approximation for the exchange-correlation functional. We use Materials Project[31] recommended projector augmented-wave atom potentials for all species and set a cutoff energy of 520 eV for the plane-wave basis set. Reciprocal space sampling was performed using k-point meshes with 1,000 k-points per reciprocal atom. We perform spin-polarized calculations and find that the net magnetic moment is close to zero for all structures. Owing to the use of consistent calculation settings, the calculated energies can be directly compared with the data in the Materials Project database. For select compounds, the band structure is further calculated along high-symmetry directions (Fig. S5).

Synthetic details

For a typical reaction, Cu_2O and a source of an elemental chalcogen (Q) in the ratio of Q/Cu = 3 were mixed with a flux of LiOH/LiCl or AOH/AI (A = Na, K and Rb). For Li-modulated flux of AOH/AI, either LiOH or LiI was added to reach the intended A/Li ratio and hydroxide concentration, [OH] = mol(OH)/[mol(OH) + mol(X)]. The flux to reactant molar ratios were about 5–10 to ensure complete initial dissolution. Hence, for each A = Na, K and Rb, there were three synthetic parameters: temperature, [OH] and A/Li. As described in our previous work[18], we found that the ratio of Cu and Q did not affect the results, as long as Q was in excess. Furthermore, with the hydroxide fluxes, molten AOH allow in situ formation of A_2Q by disproportionation of chalcogens (through $6A\mathrm{OH} + 3Q \rightarrow 2A_2Q + A_2QO_3 + 3H_2O$), obviating a separate synthesis for A_2Q. This greatly increased the efficiency for our exploratory synthesis, allowing us to cover wider phase regions in a shorter time, as the preparation of A_2Q is not trivial and can be time-consuming. Synthesis of chalcogenides by reduction of QO_2 using As_2O_3 (ref. [32]) is also reported in hydroflux, in which hydroxides are mixed with water in a semi-closed system[33,34]. This greatly increased the efficiency of this synthesis strategy, permitting it to cover substantially wider phase regions in a shorter time. We also note that the effective flux medium is hydroxide, not halide, as the solubility of chalcogenides or oxides is much lower in halides compared with hydroxides. Reactions in halides without the presence of hydroxides only afforded binaries below 600 °C, identical to solid-state reactions.

Phase selection using this rationale method will be more straightforward because there are only two determining factors for solubility: temperature and flux ratio. Therefore, for any particular A, M and Q in $A_xM_yQ_z$, the expected phase diagram is a function of temperature and basicity, as demonstrated by the results shown in Fig. 1b,c. This provides control over and predictability of composition and dimensionality and reduces the chance of forming trivial binary phases owing to the high solubility of binaries. These reaction conditions can substantially increase the efficiency of steering the reaction paths towards new phases. Furthermore, when the solubility is sufficiently high to synthesize ternaries, they can feed on the formation of quaternary or quinary systems composed of several anions having low solubilities.

The question is how well the ability to control the solubility and concentration of building blocks facilitates the formation and selection of new compounds. We conducted our study on Cu-Q (Q = S and Se), using Cu_2O and elemental Q as the Cu and chalcogenide sources, respectively, in mixed AOH/AX (A = Li, Na, K or Rb; X = Cl or I), in which AOH was the alkaline component that enhanced the solubility and AX was used to modulate the solubility. Therefore, it is important to note that the effective medium of the flux is the hydroxide, not the halide, because the solubility of chalcogenides or oxides is much lower in halides. Although halides do not compete with chalcogenides for late transition metals, as they have been used as fluxes for growing chalcogenide crystals[35], we found that they can be combined with alkali metals to form several anion systems of (M-Q)/(A-O-X) under certain conditions using mixed hydroxide/halide fluxes. We selected Cu as a chalcophilic element because Cu-Q bonding can be favoured, even in extremely high concentrations of OH. To cover a larger phase space, we used mixed (Li, Na)OH/NaI, (Li, K)OH/KI and (Li, Rb)OH/RbI fluxes to allow the change in solubility with the AOH/AX ratio and temperature to be continuous. Subsequently, we introduced Ba in the form of BaO into the flux system to study the chemical perturbations caused by the introduction of further electropositive elements. The strategy proved to be effective, considering that 30 new compounds were synthesized, as listed in Table 1.

The as-purchased NaOH that we used contained about 10–15% water by weight and, when heated, we observed this water leaving the reaction and condensing at the end of the quartz tube, especially above 200 °C. We run our reactions in an open system and under nitrogen flow. This helped to protect the reaction from oxygen and drive off the water. In molten hydroxides, such equilibrium exists: $2OH^- \leftrightarrow H_2O + O^{2-}$, in which H_2O and O^{2-} serve as the acid and base, respectively[22,23]. Under our conditions, water cannot be trapped during the reaction, to become a very different type of flux, known as the hydroflux[33,34]. However, water can leave the fluxes, because we use an open system under constant N_2 flow. In hydroxide fluxes, the dissociation constant is defined as $K_d = [H_2O][O^{2-}]$ (ref. [36]). As K_d is a function of temperature for a given base, the minimal residual water will always be the same for given conditions. The excess water will be evaporated in such an open system under nitrogen flow, as we observed water condensing at the end of the quartz tube and leaving the reaction when the furnace temperature exceeds 200 °C. Therefore, although the NaOH precursor that we used contained about 10–15% water, the initial amount of water in the flux is not a determining factor for the results. We acknowledge that, during the crystal growth stage, the oxoacidity of the flux can change over time owing to loss of water in an open system under nitrogen flow. However, this process is suppressed by the high initial $[O^{2-}]$ resulting from dissolved Cu_2O, BaO and disproportionation of Q.

The reactants were typically in the ratio of Q/Cu = 3 and the reactant to flux ratio is around 0.1–0.2. The total mass of the flux is about 0.8–1.0 g for the 3-ml glassy carbon boats. The reaction mixture was loaded in a rectangular glassy carbon boat that was then placed inside a fused silica tube with each end connected to a metal valve to allow nitrogen gas to flow through. The fused silica tube was placed inside a tube furnace heated to 400–600 °C at a heating rate of 5 °C min^{-1}. The temperature was held for 20 h and then the furnace was cooled to 300 °C at a rate of 3–6 °C h^{-1}, followed by turning off the power. The products were washed with methanol in an ultrasonication bath to remove the flux. The disproportion of Q led to side products such as A_2QO_x (x = 3 or 4), which could be fully dissolved and removed by further rinsing with water. Although it takes more rounds of washing to remove them with methanol, it is preferred over water if the product is sensitive to moisture.

Li does not form ternaries with Cu/Q, as reactions in the flux of LiOH/LiCl only yielded various known $Cu_{2-x}Q$ binaries, except for reactions at 600 °C with Q = Se, which afforded an unknown crystal indexed to the $P3m$ space group with a = 4.07 Å and c = 9.05 Å (Fig. S6). Therefore, LiOH could be a good solubility modulator without affecting the results by direct participation of the reactions. However, we did notice that Li substitutes tetrahedrally coordinated Cu. We will also demonstrate how to control Li substitution with our flux reaction, which may be desirable for certain applications, such as direct band gap semiconductors with high Li content for neutron detection[37].

(Na, Li)OH/NaI

The melting point of NaOH/NaI at [OH] = 0.6 is approximately 330 °C. Consequently, further reducing [OH] will increase the melting point. Therefore, we modulated the solubility by introducing Li^+ into the solution to avoid reducing [OH]. For such reactions, NaOH and LiOH were combined with NaI, or Li_2O was added to a mixture of NaOH and NaI to achieve the desired [OH] and Na/Li ratios. For Q = Se in NaOH/NaI at 450 °C, the product obtained was pure **I** ($Na_{4+x}OCu_4Se_4$) for [OH] = 0.85 in the absence of Li. However, at Na/Li = 3, the products obtained were a mixture of **II** ($Na_{10+x}O_2Cu_{11+x}Se_{10}$) and **III** ($Na_{5+x}OCu_8Se_6$) at [OH] = 0.85 (Fig. S7a). Also, at Na/Li = 3, when [OH] was reduced to 0.75, the fraction of **III** ($Na_{5+x}OCu_8Se_6$) increased greatly (Fig. S7b). Furthermore, when the temperature was increased to 500 °C, the product became pure **II** with no trace of **III** (Fig. S7c). When Na/Li was reduced to 2 and [OH] to 0.75 at 450 °C, the products obtained were mainly **X** ($NaCu_3Se_2$), with the presence of an unreported minor phase having the composition of $NaCu_5Se_3$ (Fig. S8), probably isostructural to the ps-1D $NaCu_5S_3$ (ref. [38]). These results indicate that higher temperature and solubility favour products having lower dimensionality in the ternary flux of (Na, Li)OH/NaI.

At Na/Li ratios of 1 or lower, reactions at 450–600 °C, produced 2D $Na(Cu_{0.6}Li_{0.4})Se$ (**XIII**), a derivative of NaCuSe (ref. [39]), wherein large Li substitution occurred on the Cu site. We attribute the stabilization of this 2D structure instead of a 1D structure such as **I**–**III** to the higher entropy of mixing caused by Li/Cu substitution, which led to a reduction in the solubility of $Na(Cu_{0.6}Li_{0.4})Se$ (**XIII**) compared with that of the parent NaCuSe. We explain this effect in the 'Additional experimental details' section of the Supplementary Information and correlate x (the fraction of Cu substituted for Li) with temperature and solubility. Also, the overall alkali metal (Na + Li) to Cu ratio (2.33) was much higher than that of **I**–**III** (0.7–1.1).

Similar effects to the selenide systems were observed for sulfides, as increasing Li ratios generally increased the dimensionality of the products. For the reaction at 500 °C in NaOH/NaI, the product was **IV** ($Na_{4+x}OCu_4S_4$) for [OH] = 0.68 in the absence of Li. However, at Na/Li = 1, the product was **IX** ($NaCu_3S_2$), as shown in Fig. S9, which has a structure similar to that of **X** ($NaCu_3Se_2$), as shown in Fig. 1e. Compound **X** is a derivative of **IX** ($NaCu_3S_2$) exhibiting higher lattice distortion, with the symmetry being reduced from $R\text{-}3m$ to $C2/m$ (Table 1). Notably, when using the NaOH/NaI flux, **IX** ($NaCu_3S_2$) was not observed until [OH] was reduced to 0.6 and T to 400 °C. The ability of Li to modulate the solubility is pronounced. As well as pure **IX** ($NaCu_3S_2$) produced using the Li-modulated NaOH/NaI flux, the crystals obtained at higher temperatures were larger and of much higher quality. This permitted us to determine the crystal structure. For a similar reaction performed at 500 °C with Na/Li ≈ 1 and [OH] = 0.89, the product changed from **IX** ($NaCu_3S_2$) to **XII** ($Na(Cu_{0.6}Li_{0.4})S$). Despite both of these being 2D structures, **XII** is probably more favourable owing to the higher Na/Cu ratio. These observations match those of Se, except that the crystals of the sulfide analogues **IX** and **X** are larger and of higher quality, possibly because of the higher solubility of the sulfides. The crystals of **XII** ($Na(Cu_{0.6}Li_{0.4})S$) were up to 5 mm in size, which facilitated electron energy loss spectroscopy to confirm Li substitution (Fig. S10).

KOH/KI and (K, Li)OH/KI

Because the solubility greatly increases when moving from NaOH to the more basic KOH, reactions performed at [OH] > 0.6 in KOH/KI at 450 °C or higher generally resulted in metallic Cu and minor unknown phases composed of minuscule crystals unsuitable for synchrotron X-ray diffraction studies. Hence, LiOH was added to KOH to prevent the reduction of Cu^+ and enable the crystallization of chalcogenides. As shown in Extended Data Fig. 1a, for the flux composed of (K, Li)OH/KI, at [OH] = 0.85, K/Li = 0.15 and 500 °C, the product was **XXV** (KCu_5Se_3), which is unreported and isostructural with $CsAg_5Te_3$ (ref. [40]). Compared with the 1D and 2D compounds prepared using NaOH/NaI, this compound has a ps-1D structure with K-ion-filled 1D channels defined by four chains of 3 × ∞ edge-sharing $CuSe_4$ tetrahedra. For a similar reaction with identical [OH] and T, but performed at K/Li = 3, the products were α-KCu_3Se_2 (Extended Data Fig. 1b), which has a 2D structure[41], and an unknown phase exhibiting a broad peak at 10.6° (Fig. S11a). When [OH] was reduced to 0.7, the unknown phase disappeared, and only α-KCu_3Se_2 (Fig. S11b) remained, implying that this unknown phase is favoured at high solubilities.

At [OH] = 0.7 and 450 °C, the primary product was another 2D layered structure[42] $K_3Cu_8Se_6$ (Extended Data Fig. 1c and Fig. S11c). When K/Li was increased to 6 and T to 400 °C, the reaction produced a mixture of $K_3Cu_8Se_6$ and KCu_2Se_2 (ref. [43]) (Extended Data Fig. 1d). Because KCu_2Se_2 possesses a higher K/Cu ratio (0.5) than $K_3Cu_8Se_6$ (0.375), it is probable that the effect of increasing [KOH] was stronger than that of reducing the temperature. Consequently, the equilibrium shifted marginally towards KCu_2Se_2, resulting in a mixture with $K_3Cu_8Se_6$. For reactions in KOH/KI in the absence of Li at 450 °C, the main product obtained following washing with methanol was metallic Cu. However, some air-sensitive needle-shaped crystals were observed on top of the flux before washing and were indexed to an $I4/m$ space group with a = 11.5540(16) Å and c = 4.3985(9) Å, which is assigned as $K_{4+x}OCu_4Se_4$ (**VIII**, Extended Data Fig. 1e), a K-analogue of $Na_{4+x}OCu_4Se_4$ (**I**). Similarly, from **b** to **e** as shown in Extended Data Fig. 1, at K/Li higher than 3, the unknown phase (Fig. S11a) is also **VIII** ($K_{4+x}OCu_4Se_4$). These results demonstrate that lower dimensionality and higher A/Cu ratios are favoured at higher solubilities, which agrees with the results obtained when using NaOH/NaI as the flux.

For Q = S, **XI** (KCu_3S_2, Extended Data Fig. 1f), which is an unreported compound and isostructural to **IX** ($NaCu_3S_2$), was obtained at 600 °C, [OH] = 0.8 and K/Li = 1 (Fig. S12a). When K/Li was increased to 2 but the temperature was reduced to 450 °C, the product obtained was **VII** ($K_{4+x}OCu_4S_4$, Extended Data Fig. 1e), which was indexed to the $I4/m$ space group with a = 11.1980(4) Å and c = 4.068(3) Å, and is probably an analogue of $Na_{4+x}OCu_4S_4$. However, at K/Li = 2, when the temperature was not reduced to 450 °C, the Cu_2O precursor was particularly reduced to metallic Cu. Hence, KOH seems to exert a much stronger effect than NaOH. At K/Li = 1 and [OH] = 0.8, when the reaction was carried out at 400 °C instead of 600 °C for **XI** (KCu_3S_2, Extended Data Fig. 1f), the product obtained was α-KCu_3S_2 (ref. [44]) (Extended Data Fig. 1g and Fig. S12b), which is isostructural to the Se analogue, as shown in Extended Data Fig. 1b. Therefore, the trend of favouring products having lower dimensionality with increasing temperature and solubility holds.

(Rb, Li)OH/RbI

The solubility of the reactants was greater in the flux composed of RbOH/RbI than that in KOH/KI; therefore, we reduced it by using a Li-modulated flux of (Rb, Li)OH/RbI. This produced an unreported compound, **XXVI** ($RbCu_{7-x}Se_4$), that has a unique structure (Extended Data Fig. 2a) at [OH] = 0.75 and Rb/Li = 2 at 450 °C. This compound has infinite 1D channels enclosed by four chains of 2 × ∞ edge-sharing $CuSe_4$ tetrahedra instead of 3 × ∞ as seen in **XXV** (KCu_5Se_3). The complete occupation of the Cu site would yield a formula of $RbCu_8Se_4$. However, with unfilled Cu vacancies, the actual formula is $RbCu_{6.1}Se_4$, suggesting formal Cu-ion mixed valence. When Rb/Li was increased from 2 to 4, the product obtained was 2D layered $Rb_3Cu_8Se_6$ (Extended Data Fig. 2b and Fig. S13a) instead of ps-1D **XXVI** ($RbCu_{7-x}Se_4$). When the temperature was increased to 500 °C and Rb/Li decreased to 0.35, the product was 2D $RbCu_4Se_3$ (Fig. S13b), consisting of thicker anti-PbO layers of Cu_4Se_3, as shown in Extended Data Fig. 2c. Therefore, the dimensionality decreases here as well with increasing basicity, temperature and solubility.

0D cluster of $Ba_4Rb_6Cu_{12}Se_{13}$

The suggested reaction paths formed the unique 0D compound $Ba_4Rb_6Cu_{12}Se_{13}$ (**XXVII**) together with the above-mentioned 1D, 2D and ps-1D compounds (Fig. 2l). It was formed with **XXVI** ($RbCu_{7-x}Se_4$) when BaO was present at [OH] = 0.75 and Rb/Li = 2 at 450 °C. It has discrete $Cu_{12}Se_{13}$ icosahedral clusters. There are 20 tetrahedral sites formed by Se(1) and Se(2), and 12 Cu atoms occupy every other tetrahedral site such that Cu–Cu interactions can be prevented. Although copper chalcogenide clusters have been widely reported, this is the first time such a cluster has formed in solution without organic ligands[45]. Its stabilization indirectly shows the nature of dissolved species and the potential building blocks present in these solutions. Knowledge gained by further investigating the cluster compounds under different conditions may help to understand the molecular mechanisms of these reactions.

It is probable that this compound was not formed at the crystallization temperature of 450 °C because a higher-dimensional compound, $RbCu_{7-x}Se_4$ (**XXVI**), was also formed. If the solubility of the flux using RbOH is excessive, the solution may never saturate and precipitate chalcogenides. However, when the solution was cooled to below the melting point, all solutes crystallized immediately with the surrounding ions. It is possible that this icosahedral cluster was the exact coordination environment for Cu–Se immediately before freezing the solution. This was evidenced by the small and irregular size of the $Ba_4Rb_6Cu_{12}Se_{13}$ (**XXVII**) crystals. We found that much smaller yellow particles were also obtained when using high [OH] with KOH/KI and NaOH/NaI, but they readily dissipated during ultrasonication in methanol. These may also be cluster compounds having a much smaller crystal size. The stabilization of $Ba_4Rb_6Cu_{12}Se_{13}$ (**XXVII**) over the products using KOH and NaOH may be a result of the large cationic size of Rb^+ and high ionic charge of Ba^{2+}.

Panoramic synthesis

We carried out the following panoramic syntheses using in situ PXRD at 17-BM at the Advanced Photon Source (APS): (1) NaOH/NaI with [OH] = 0.60, Q = Se; (2) NaOH/NaI with [OH] = 0.8, Q = Se; (3) (Na, Li)OH/NaI with [OH] = 0.60, Q = Se, Na/Li = 3; (4) NaOH/NaI with [OH] = 0.7, Q = S; (5) NaOH/NaI with [OH] = 0.65, Q = S and further BaO. The results for reactions (1)–(3) and (5) are shown in Extended Data Fig. 3 and the corresponding temperature profiles are shown in Fig. S3. The results for reaction (4) is shown in Fig. S4.

For all reactions, we saw that NaOH started to disappear around 70 °C. We observed the formation of an unknown phase A (marked in Extended Data Fig. 3a–c) with a narrow stability window between 70 and 160 °C for reactions (1)–(3). Unknown A is probably a metastable phase that dissolves completely above 160 °C, which is why it has not been observed for any of the ex situ reactions. For reaction (2) with low [OH] = 0.60, the initial product was **II** ($Na_{10+x}O_2Cu_{11+x}Se_{10}$) at lower temperatures between 200 and 400 °C but quickly converted to **I** ($Na_{4+x}OCu_4Se_4$) completely before reaching 450 °C. No phase change was observed after that heating to 600 °C, at which **I** started to convert to **X** ($NaCu_3Se_2$) and almost completed after reaction for 3 h at 550 °C. The conversion from **II** to **I** with increasing temperature is similar to what was observed for ex situ reactions, in which higher temperature favours higher Na/Cu ratios and lower dimensionality. However, compared with our ex situ reactions, the formation of the heterochained products such as **I** or **II** were surprising for such low [OH] at 0.60. In comparison, the as-recovered products during ex situ reactions were **III** or **X**. It is important to note that the isothermal stage of the reaction was 20 h for ex situ synthesis, whereas the timescale was much shorter for the in situ ones (<3 h). Therefore, the reactions for in situ studies may not have reached completion and kinetic effects cannot be ignored. The initial formation of **II** or **I** might be due to higher [OH] than intended, as NaI was not fully dissolved owing to its high melting point compared with NaOH. This is supported by the PXRD patterns shown in Extended Data Fig. 3a, as NaI was present until 600 °C, whereas NaOH completely disappeared before 200 °C. This also explains why when more NaI went into the solution at higher temperatures above 500 °C, **I** ($Na_{4+x}OCu_4Se_4$) started to convert to **X** ($NaCu_3Se_2$), a higher-dimension product. The conversion from **I** to **X** was complete after holding at 600 °C for 2 h. This is consistent with our observation for ex situ reactions.

For reaction (2) with higher [OH] at 0.8, the initial product was **II** (mixed chain) at lower temperatures but quickly converted to **I** (single chain) completely before reaching 450 °C, and no phase change was observed thereafter for reactions up to 550 °C (Extended Data Fig. 3b). Because the [OH] remained high for this reaction, unlike reaction (1), no conversion to **X** was observed. A similar reaction for Q = S described in reaction (4) (Fig. S4) also resulted in the single-chained product, **IV** ($Na_{4+x}OCu_4S_4$), an analogue of **I**.

The reaction for even lower solubility (basicity) with (Na, Li)OH/NaI of reaction (3) is even more interesting, as shown in Extended Data Fig. 3c. We observed **II** between 200 and 400 °C, which converted to **I** at 450 °C. When heated above 500 °C, **I** started converting to **X**. When heated from 550 °C, both **I** and **X** converted to a new phase C with an unknown intermediate B. When the temperature was raised to 600 °C, C converted to another unknown D, which reverted back to C during cooling. We solved the structure of C by picking out the single crystal from the reaction, which is a new phase $Na_3Cu_4Se_4$ isostructural to $K_3Cu_4S_4$ (ref. [46]). Therefore, we give the code name **XXVIII** to the unknown C. We also found red crystals of D, which was indexed to a trigonal crystal system with a = 3.038(14) Å and c = 7.429(60) Å by single-crystal diffraction. Its lattice constant c agrees with the Bragg peak marked in the yellow box shown in Extended Data Fig. 3c. Therefore, it is probable that the red crystals were the unknown D. However, owing to the small size of its crystals (<20 μm), we were not able to solve its structure.

For reaction (5) (NaOH/NaI with [OH] = 0.65, Q = S) with BaO as the perturbation, several intermediate phases such as E, F and G marked on Extended Data Fig. 3d appeared before reaching 400 °C. We also observed the formation of **V** ($Na_{10+x}O_2Cu_{11+x}S_{10}$) at around 250 °C. It converted to **IV** ($Na_{4+x}OCu_4S_4$) above 400 °C, the only phase when the temperature was held at 400 °C for 1 h. However, when heating from 400 °C to 450 °C, **IV** was completely dissolved. This is surprising, as no complete dissolution was observed for reaction (4) with [OH] = 0.7 (Fig. S4), indicating higher dissolving power of the flux with the addition of BaO. When the temperature was held at 450 °C, **XVI** ($Na_3BaCu_7S_6$) started to crystallize and the intensities of its reflection increased over time. With more **XVI** ($Na_3BaCu_7S_6$) formed at 450 °C over time, the dissolving power of the flux reduced as well. As a result, **IV** ($Na_{4+x}OCu_4S_4$) re-emerged as shown in Extended Data Fig. 3d. When cooled to room temperature from 450 °C, two more previously unidentified phases H and I were observed (Extended Data Fig. 3d).

Now, with a better understanding of the chemistry, we demonstrate how we can rationally tune the properties of materials. Both the $K_3Cu_4S_4$-type[46] and $Rb_3Cu_8Se_6$-type[47] structures are metallic, owing to extra holes in their valence bands. The traditional solid-state method cannot produce electron-precise semiconducting products for these structural types. They contain hole carriers delocalized in Cu-d and Q-p orbital states. Because these mixed-valence compounds are mainly formed with low solubility at lower temperatures or [OH], we targeted $BaK_2Cu_4S_{4-x}Se_x$ (x = 2) (**XXIX**) by slightly increasing the temperature to 600 °C from 550 °C (compared with the condition of **XXVIII** shown in Table 1) with Li/K = 3 and Cu_2O/BaO = 2 in a (Li, K)OH/KI flux with [OH] = 0.7. DFT band-structure calculations show that $BaK_2Cu_4S_4$ and $BaK_2Cu_4Se_4$ are direct band gap (E_g) semiconductors (Fig. S5a,b), respectively, for which these phases are electron precise. $BaK_2Cu_4S_{4-x}Se_x$ is a tunable direct band gap semiconductor whose E_g decreases with increasing x. Similarly, we targeted and obtained $BaK_2Cu_8S_6$ (**XXX**) with a LiOH/KOH flux (Li/K = 9) at 450 °C, which is also a direct band gap semiconductor, with E_g = 0.5 eV (Fig. S5c).

As well as the phase-selection mechanism, panoramic synthesis experiments also show aspects of the crystal-growth mechanism. As shown in Extended Data Fig. 3, once the flux is molten, most materials dissolve quickly (whether completely dissolved or not, depending on the ratio of reactant/flux) and start to precipitate immediately, just as with solution reaction. Even during the isothermal reaction period, the powder Bragg rings became grainier over time (2D diffraction patterns shown in Fig. 3a). For example, for the reaction of Ba/Cu/S in NaOH/NaI, we see at 400 °C that the powder pattern was well-formed Bragg rings after about 1 h of reaction, indicating very tiny crystallites.

When heated to 450 °C from 400 °C, all solids dissolved and no Bragg diffraction ring is visible. However, after reacting for 1 h, we started to see grainier spots, which became more grainy after 1.5 h, indicating crystal growth over time. When the reaction was cooled to 225 °C at a rate of 15 °C min^{-1}, we saw much larger spots, showing crystal growth by cooling.

These observations are consistent with our ex situ synthesis and we have observed that the grown crystals are generally larger with higher reaction temperature and longer reaction time. These crystals evidently served as seeds and grew even larger during cooling. Therefore, to produce larger crystals, we can set the growth temperature as high as possible (without changing to a different phase) for a reaction period that reaches growth equilibrium, usually >20 h. Then, we can apply thermal oscillation to the system by cooling by 50–100 °C slowly at a rate of 3–10 °C h^{-1} and quickly heating to the set temperature at 100–300 °C h^{-1} and repeating for several cycles before cooling it to room temperature. The thermal oscillation process allows smaller crystallites formed during cooling to be re-dissolved and large crystals to grow larger.

Data availability

Crystallographic data for the structures reported in this article have been deposited at the Cambridge Crystallographic Data Centre, with deposition numbers 2184424–2184451, corresponding to compounds shown in Table 1: **I** ($Na_{4+x}OCu_4Se_4$, CSD 2184424), **II** ($Na_{10+x}O_2Cu_{11+x}Se_{10}$, CSD 2184425), **III** ($Na_{5+x}OCu_8Se_6$, CSD 2184427), **IV** ($Na_{4+x}OCu_4S_4$, CSD 2184435), **V** ($Na_{10+x}O_2Cu_{11+x}S_{10}$, CSD 2184429), **VI** ($Na_{5+x}OCu_8S_6$, CSD 2184433), **VIII** ($K_{4+x}OCu_4Se_4$, CSD 2184438), **IX** ($NaCu_3S_2$, CSD 2184426), **X** ($NaCu_3Se_2$, CSD 2184428), **XII** ($Na(Cu_{0.6}Li_{0.4})S$, CSD 2184430), **XIII** ($Na(Cu_{0.6}Li_{0.4})Se$, CSD 2184431), **XIV** ($BaCu_{1.4}Li_{0.6}S_2$, CSD 2184436), **XV** ($(Ba_{0.44}Rb_{0.56})Cu_2Se_2$, CSD 2184441), **XVI** ($Na_3BaCu_7S_6$, CSD 2184432), **XVII** ($K_3BaCu_7S_6$, CSD 2184434), **XVIII** ($Ba_2Cu_2Na_{1.3}O_{1.1}S_3$, CSD 2184442), **XIX** ($Ba_{4.5}Cu_{6.7}Na_{1.7}O_4S_6$, CSD 2184439), **XX** ($Ba_{2-x}Cu_{5.5}OSe_4$, CSD 2184437), **XXI** ($Ba_2Cu_{0.8}O_2Cu_2Se_2$, CSD 2184443), **XXII** ($Ba_2Na_{0.55}O_2Cu_2Se_2$, CSD 2184440), **XXIII** ($(Ba_{1.63}K_{0.37})O_2Cu_2Se_2$, CSD 2184445), **XXIV** ($Ba_2Cu_{0.8}O_3CuS$, CSD 2184450), **XXV** (KCu_5Se_3, CSD 2184444), **XXVI** ($RbCu_{7-x}Se_4$, CSD 2184448), **XXVII** ($Ba_4Rb_6Cu_{12}Se_{13}$, CSD 2184447), **XXVIII** ($Na_3Cu_4Se_4$, CSD 2184446), **XXIX** ($BaK_2Cu_4S_{4-x}Se_x$, CSD 2184451), **XXX** ($BaK_2Cu_8S_6$, CSD 2184449). Copies of the data can be obtained free of charge at https://www.ccdc.cam.ac.uk/structures/. Source data for Extended Data Fig. 3 is provided within this paper. Data are also available on request. Source data are provided with this paper.

27. Kresse, G. & Furthmüller, J. Efficient iterative schemes for ab initio total-energy calculations using a plane-wave basis set. *Phys. Rev. B* **54**, 11169–11186 (1996).
28. Blöchl, P. E. Projector augmented-wave method. *Phys. Rev. B* **50**, 17953–17979 (1994).
29. Kresse, G. & Joubert, D. From ultrasoft pseudopotentials to the projector augmented-wave method. *Phys. Rev. B* **59**, 1758–1775 (1999).
30. Perdew, J. P., Burke, K. & Ernzerhof, M. Generalized gradient approximation made simple. *Phys. Rev. Lett.* **77**, 3865–3868 (1996).
31. Jain, A. et al. Commentary: The Materials Project: a materials genome approach to accelerating materials innovation. *APL Mater.* **1**, 011002 (2013).
32. Albrecht, R. & Ruck, M. Chalcogenides by reduction of their dioxides in ultra-alkaline media. *Angew. Chem. Int. Edn* **60**, 22570–22577 (2021).
33. Bugaris, D. E., Smith, M. D. & zur Loye, H.-C. Hydroflux crystal growth of platinum group metal hydroxides: $Sr_6NaPd_2(OH)_{17}$, $Li_2Pt(OH)_6$, $Na_2Pt(OH)_6$, $Sr_2Pt(OH)_8$, and $Ba_2Pt(OH)_8$. *Inorg. Chem.* **52**, 3836–3844 (2013).
34. Chance, W. M., Bugaris, D. E., Sefat, A. S. & zur Loye, H.-C. Crystal growth of new hexahydroxometallates using a hydroflux. *Inorg. Chem.* **52**, 11723–11733 (2013).
35. Klepov, V. V., Juillerat, C. A., Pace, K. A., Morrison, G. & zur Loye, H.-C. "Soft" alkali bromide and iodide fluxes for crystal growth. *Front. Chem.* **8**, 518 (2020).
36. Mugavero III, S. J., Gemmill, W. R., Roof, I. P. & zur Loye, H.-C. Materials discovery by crystal growth: lanthanide metal containing oxides of the platinum group metals (Ru, Os, Ir, Rh, Pd, Pt) from molten alkali metal hydroxides. *J. Solid State Chem.* **182**, 1950–1963 (2009).
37. Chica, D. G. et al. Direct thermal neutron detection by the 2D semiconductor $^6LiInP_2Se_6$. *Nature* **577**, 346–349 (2020).
38. Effenberger, H. & Pertlik, F. Crystal structure of $NaCu_5S_3$. *Monatsh. Chem. Chem. Mon.* **116**, 921–926 (1985).
39. Savelsberg, G. Ternäre Pnictide und Chalkogenide von Alkalimetallen und IB-bzw. IIB-Elementen/On ternary pnictides and chalcogenides of alkaline metals and IB-resp. II B-elements. *Z. Naturforsch. B* **33**, 370–373 (1978).
40. Li, J., Guo, H.-Y., Zhang, X. & Kanatzidis, M. G. $CsAg_5Te_3$: a new metal-rich telluride with a unique tunnel structure. *J. Alloys Compd.* **218**, 1–4 (1995).
41. Rettie, A. J. E. et al. Copper vacancies and heavy holes in the two-dimensional semiconductor $KCu_{3-x}Se_2$. *Chem. Mater.* **29**, 6114–6121 (2017).
42. Näther, C., Röhnert, D. & Bensch, W. Synthesis, crystal structure and low-temperature X-ray investigations of $K_3Cu_8Se_6$. *Eur. J. Solid State Inorg. Chem.* **35**, 565–577 (1998).
43. Tiedje, O. et al. Bridging from $ThCr_2Si_2$-type materials to hexagonal dichalcogenides: an *ab initio* and experimental study of KCu_2Se_2. *Phys. Rev. B* **67**, 134105 (2003).
44. Burschka, C. & Bronger, W. KCu_3S_2, ein neues Thiocuprat/KCu_3S_2, a new thiocuprate. *Z. Naturforsch. B* **32**, 11–14 (1977).
45. Fuhr, O., Dehnen, S. & Fenske, D. Chalcogenide clusters of copper and silver from silylated chalcogenide sources. *Chem. Soc. Rev.* **42**, 1871–1906 (2013).
46. Shoemaker, D. P. et al. In situ studies of a platform for metastable inorganic crystal growth and materials discovery. *Proc. Natl Acad. Sci. USA* **111**, 10922–10927 (2014).
47. Schils, H. & Bronger, W. Ternäre Selenide des Kupfers. *Z. Anorg. Allg. Chem.* **456**, 187–193 (1979).

Acknowledgements This work was supported by the U.S. Department of Energy, Office of Science, Basic Energy Sciences, Materials Sciences and Engineering Division. Work carried out at the Center for Nanoscale Materials (SEM, ACAT and Carbon high-performance computing cluster), a US Department of Energy (DOE) Office of Science User Facility, was supported by the US DOE Office of Basic Energy Sciences under contract no. DE-AC02-06CH11357. The computational work is supported by the US DOE Office of Science Scientific User Facilities AI/ML project titled 'A digital twin for spatiotemporally resolved experiments.' M.K.Y.C. acknowledges support from the BES SUFD Early Career award. Work at the beamlines 15-IDD and 17-BM at the Advanced Photon Source (APS) at Argonne National Laboratory was supported by the US DOE, Office of Science, Office of Basic Energy Sciences under contract no. DE-AC02-06CH11357. NSF's ChemMatCARS Sector 15 is supported by the Divisions of Chemistry (CHE) and Materials Research (DMR), National Science Foundation, under grant no. NSF/CHE-1834750.

Author contributions The work was conceived by X.Z., D.-Y.C. and M.G.K., with input from all authors. X.Z. carried out the synthesis, lab X-ray diffraction and elemental analysis. X.Z. and W.X. collected and analysed in situ synchrotron diffraction data. V.-S.-C.K., L.W. and M.K.Y.C. performed first-principle calculations. X.Z., T.C. and Y.-S.C. collected and analysed single-crystal diffraction data. L.Y. and J.W. collected and analysed electron energy loss spectroscopy spectra. D.-Y.C. and M.G.K. supervised the project.

Competing interests The authors declare no competing interests.

Additional information

Supplementary information The online version contains supplementary material available at https://doi.org/10.1038/s41586-022-05307-7.

Correspondence and requests for materials should be addressed to Mercouri G. Kanatzidis.

Peer review information *Nature* thanks Hans Conrad zur Loye and the other, anonymous, reviewer(s) for their contribution to the peer review of this work.

Reprints and permissions information is available at http://www.nature.com/reprints.

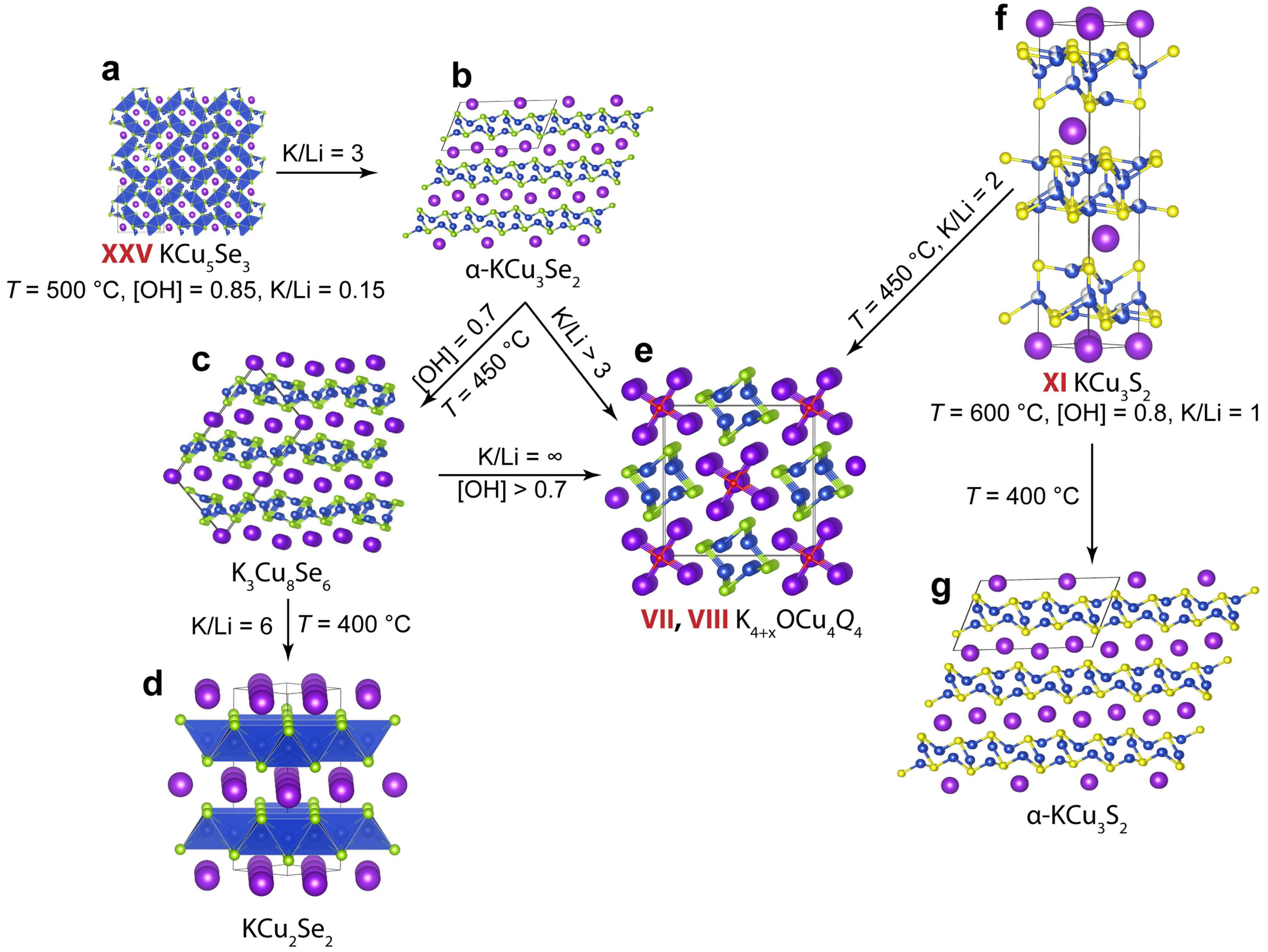

Extended Data Fig. 1 | Reaction pathways in the (K, Li)OH/KI flux. **a**, **XXV** (KCu$_5$Se$_3$). **b**, α-KCu$_3$Se$_2$. **c**, K$_3$Cu$_8$Se$_6$. **d**, KCu$_2$Se$_2$. **e**, K$_{4+x}$OCu$_4$$Q_4$. **f**, **XI** (KCu$_3S_2$). **g**, α-KCu$_3S_2$. Compounds from Table 1 are shown as **VII** (K$_{4+x}$OCu$_4$S$_4$), **VIII** (K$_{4+x}$OCu$_4$Se$_4$), **XI** (KCu$_3$S$_2$) and **XXV** (KCu$_5$Se$_3$). The crystal structures **VII** and **VIII** are identical to that of **I** (Na$_{4+x}$OCu$_4$Se$_4$) and **XI** is isostructural with **IX** (KCu$_3$S$_2$). Purple, blue, red, light yellow and light green spheres represent K, Cu, O, S and Se atoms, respectively.

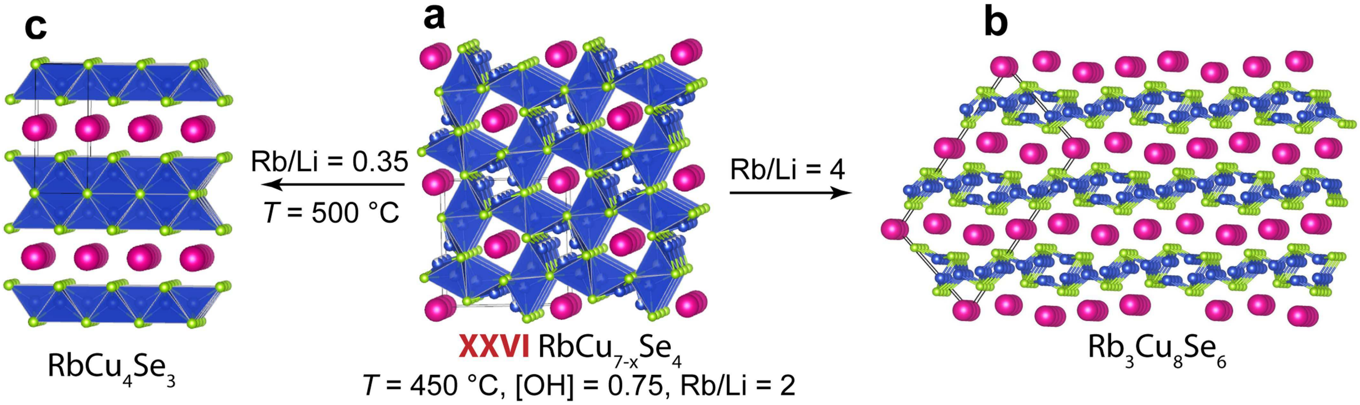

Extended Data Fig. 2 | Reaction pathways in the (Rb, Li)OH/RbI flux. **a**, $RbCu_4Se_3$. **b**, **XXVI** ($RbCu_{7-x}Se_4$). **c**, $Rb_3Cu_8Se_6$. Compounds from Table 1 are shown as **XXVI** ($RbCu_{7-x}Se_4$). Pink, blue and light green spheres represent Rb, Cu and Se atoms, respectively.

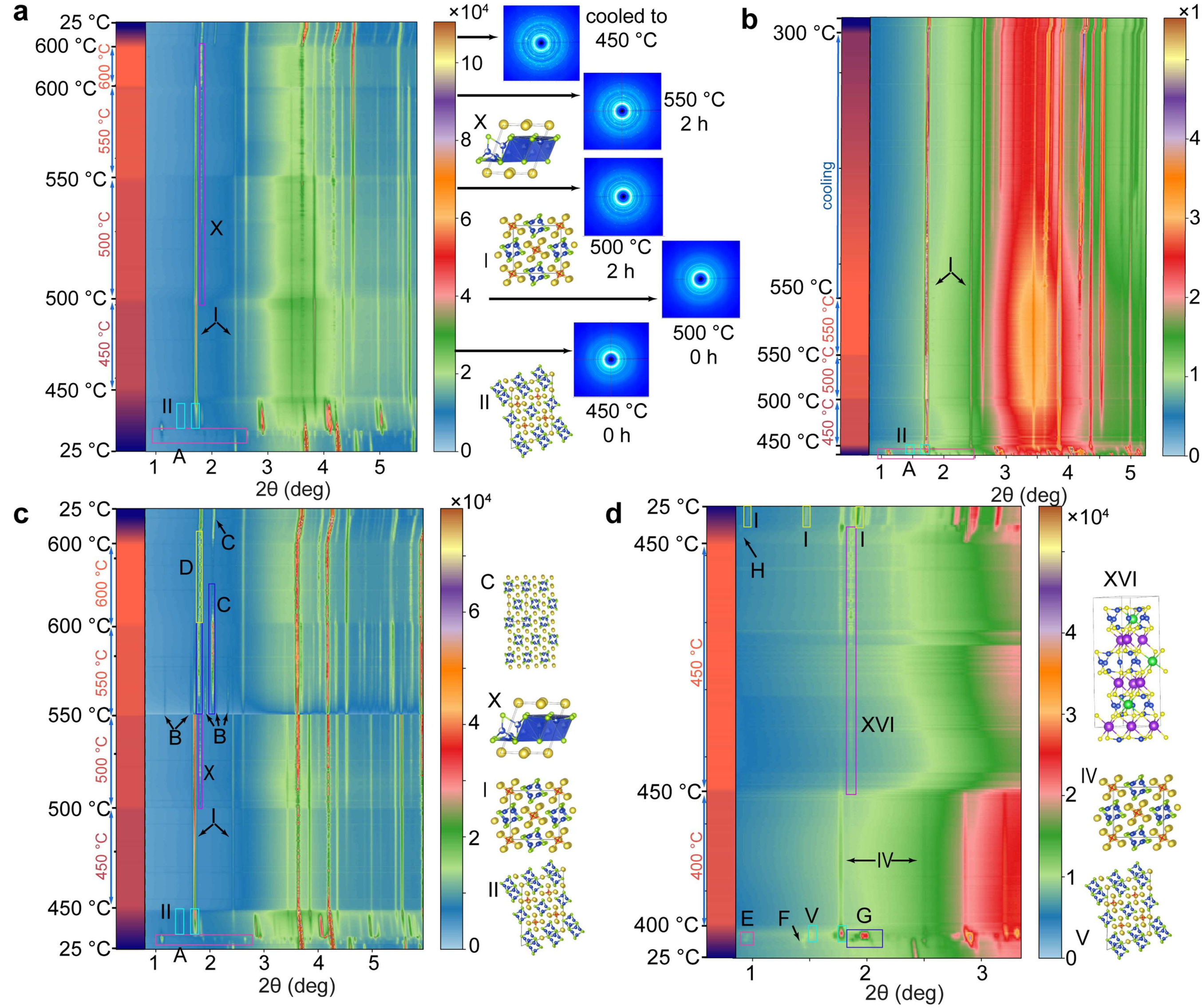

Extended Data Fig. 3 | Panoramic synthesis. In situ synchrotron powder X-ray diffraction patterns of reactions collected in the mixed flux of NaOH/NaI for [OH] = 0.60, Q = Se (**a**), [OH] = 0.80, Q = Se (**b**), [OH] = 0.80, Q = Se, Na/Li = 1 (**c**) and [OH] = 0.65, Q = S with addition of BaO (**d**). Their respective temperature profiles are shown in Fig. S3. G marked with the purple box in **d** is probably several different unknown phases with overlapping Bragg peaks.